Diffraction deep neural network based orbital angular momentum mode recognition scheme in oceanic turbulence

Hai-Chao Zhan(詹海潮)[1], Bing Chen(陈兵)[1], Yi-Xiang Peng(彭怡翔)[1], Le Wang(王乐)[1], Wen-Nai Wang(王文鼐)[2], and Sheng-Mei Zhao(赵生妹)[1,2,†]

[1] *Institute of Signal Processing and Transmission, Nanjing University of Posts and Telecommunications (NUPT), Nanjing* 210003, *China*
[2] *Key Laboratory of Broadband Wireless Communication and Sensor Network Technology (Ministry of Education), Nanjing University of Posts and Telecommunications, Nanjing* 210003, *China*

(Received 9 July 2022; revised manuscript received 13 September 2022; accepted manuscript online 21 September 2022)

Orbital angular momentum (OAM) has the characteristics of mutual orthogonality between modes, and has been applied to underwater wireless optical communication (UWOC) systems to increase the channel capacity. In this work, we propose a diffractive deep neural network (DDNN) based OAM mode recognition scheme, where the DDNN is trained to capture the features of the intensity distribution of the OAM modes and output the corresponding azimuthal indices and radial indices. The results show that the proposed scheme can recognize the azimuthal indices and radial indices of the OAM modes accurately and quickly. In addition, the proposed scheme can resist weak oceanic turbulence (OT), and exhibit excellent ability to recognize OAM modes in a strong OT environment. The DDNN-based OAM mode recognition scheme has potential applications in UWOC systems.

Keywords: orbital angular momentum, diffractive deep neural network, mode recognition, oceanic turbulence

PACS: 42.30.Sy, 42.68.–w, 42.79.Ta, 84.35.+i **DOI:** 10.1088/1674-1056/ac935e

1. Introduction

Recently, the demand for underwater wireless optical communication (UWOC) is increasing rapidly, so the communication system needs to have the characteristics of large capacity, high speed, and low delay.[1–4] UWOC has many applications in military, civilian, and commercial, such as submarines, underwater unmanned vehicles, and deep-sea resource exploration.[5–8] In 1992, Allen *et al.* exhibited that a vortex beam can carry orbital angular momentum (OAM).[9] The wavefront of the OAM beam has a helical phase and its electric field complex amplitude contains a term of $\exp[\mathrm{i}\ell\theta]$, where ℓ can be an arbitrary integer named topological charge or azimuthal index, representing the number of 2π phase shifts across the beam, and θ is the azimuthal angle. The OAM beams of different modes are orthogonal to each other,[10–13] which supports efficient multiplexing of OAM and provides a new degree of freedom for expanding the capacity of the UWOC system.[14]

In order to improve the OAM multiplexing efficiency of a UWOC system, the detection and recognition of OAM modes are crucial. There are some traditional methods, e.g., Rufato *et al.* presented computer-generated holograms (CGH) encoding information for beams carrying OAM;[15] Lei *et al.* utilized Dammann optical vortex gratings to generate, transmit and detect simultaneously independent collinear OAM channels;[16] Stegenburgs *et al.* used 3D-printed microscale spiral phase plates (SPPs) to generate OAM carrying beams.[17] These methods require guaranteed alignment of the optical path and are susceptible to factors such as turbulence, angular tilt, and lateral offset. Furthermore, most of the existing OAM based systems focus on the azimuthal index, while the radial index p, another degree of freedom of the vortex beam, has not received much attention. The radial index represents the number of rings in the radial intensity distribution of a vortex beam, which is a non-negative integer. Mazilu *et al.* used principal component analysis to simultaneously measure the azimuthal and radial indices of pure vortex light fields.[18] In 2018, Guo *et al.* established a novel OAM encoding system using a series of holograms of OAM modes with different radial indices to achieve coaxial transmission of multiplexed beams.[19] These methods consume experimental equipment and have low efficiency, especially in the complex underwater communication environment, which hinders the development of OAM-based underwater communication, so high-efficiency and low-energy solutions are needed urgently.

Now, with the gradual popularization of artificial intelligence, machine learning has been applied to many fields, including optical imaging, pattern recognition and turbulent aberration correction, etc.[20,21] In 2020, Dedo *et al.* used Gerchberg Saxton (GS) algorithm to correct the intensity distribution of the OAM beam distorted by atmospheric turbulence, then a convolutional neural network (CNN) was utilized to identify the OAM mode.[22] Lu *et al.* proposed a CNN-based model that utilizes the same backbone for OAM recognition and adaptive optics without wavefront sensor.[23] Zhang *et*

†Corresponding author. E-mail: zhaosm@njupt.edu.cn

© 2023 Chinese Physical Society and IOP Publishing Ltd

al. used intensity images generated in simulations and experiments as input data to train a neural network to recognize the OAM mode.[24] However, the neural network models in these methods are all electrically actuated, which allows the light field signal to be processed only offline. In 2018, Lin *et al.* designed an all-optical diffractive deep neural network (DDNN) using passive diffractive layers to realize various functions of deep learning.[25] DDNN works by physically creating several transmissive or reflective layers, and gives the input wave of each sensing node on each layer, the sensing node represents the neuron that connects to the next layer. The advantage of DDNN over electric deep neural network is that the diffraction layer can be solidified and fabricated to achieve the network model task at the speed of light.[26]

In this paper, we propose a DDNN-based OAM mode recognition scheme. We utilize the DDNN model to rapidly and accurately recognize the azimuthal indices and radial indices of OAM modes simultaneously. We select OAM modes with different azimuthal and radial indices, and evaluate the effects of the number of diffraction layers and different OT strengths of the DDNN model on the recognition accuracy. We verify the reliability of the proposed scheme and compare it with traditional CNN-based OAM mode recognition methods at different OT strengths.

2. Theory

2.1. DDNN-based OAM mode recognition scheme

The schematic diagram of the OAM mode recognition scheme based on DDNN is shown in Fig. 1(a). The intensity pattern of the OAM beam with azimuthal and radial indices is input to the DDNN, and then passes through a series of diffractive layers. The output plane is divided into a 4×4 grid array, where the first two rows represent the 8 different azimuthal indices of the OAM mode, and the last two rows represent the 8 different radial indices. From the location of the bright spot on the output plane, the azimuthal and radial indices of the OAM modes can be deduced. Each sensor node on the diffraction layer of DDNN is similar to the neuron in the neural network. In the process of forward propagation, each sensor node on the previous diffraction layer is fully connected to the next diffraction layer, as shown in Fig. 1(b). DDNN consists of an input layer, an output layer and several diffraction layers. According to the Rayleigh–Sommerfeld diffraction theory, each sensor node can be regarded as a secondary wave source,[27] and the optical modes can be expressed as

$$\omega_i^N(x,y,z) = \frac{z-z_i}{r^2}\left(\frac{1}{\mathrm{j}\lambda}+\frac{1}{2\pi r}\right)\exp\left(\frac{\mathrm{j}2\pi r}{\lambda}\right), \tag{1}$$

where N represents the N^{th} layer of the DDNN, i is the sensor node located at (x_i, y_i, z_i) of the N^{th} layer; r denotes the distance from the source to the i^{th} sensor node in the N^{th} layer, $r = \sqrt{(x-x_i)^2+(y-y_i)^2+(z-z_i)^2}$, $j^2 = -1$; and λ represents the wavelength. The secondary wave generated by the i^{th} sensor node can be determined by its input wave and transmission coefficient $t_i^N(x_i, y_i, z_i)$. Therefore, the output of the i^{th} sensor node in the N^{th} layer can be expressed as

$$\begin{aligned} s_i^N(x,y,z) &= \omega_i^N(x,y,z)\times t_i^N(x_i,y_i,z_i) \\ &\quad\times\sum\nolimits_k s_k^{N-1}(x_i,y_i,z_i), \end{aligned} \tag{2}$$

where $\sum_k s_k^{N-1}(x_i, y_i, z_i)$ represents the input wave superposition of all sensor nodes on the $(N-1)^{\text{th}}$ layer to the i^{th} sensor node on the N^{th} layer. The transmission coefficient consists of two parts, amplitude and phase, that is, $t_i^N(x_i, y_i, z_i) = a_i^N(x_i, y_i, z_i)\exp\left(\mathrm{j}\phi_i^N(x_i, y_i, z_i)\right)$. The DDNN model parameters are optimized by error back-propagation and stochastic gradient descent during training. According to the parameter variables in the transmission coefficient, the DDNN model can be divided into three types, including phase-only modulation, amplitude-only modulation, and hybrid modulation.

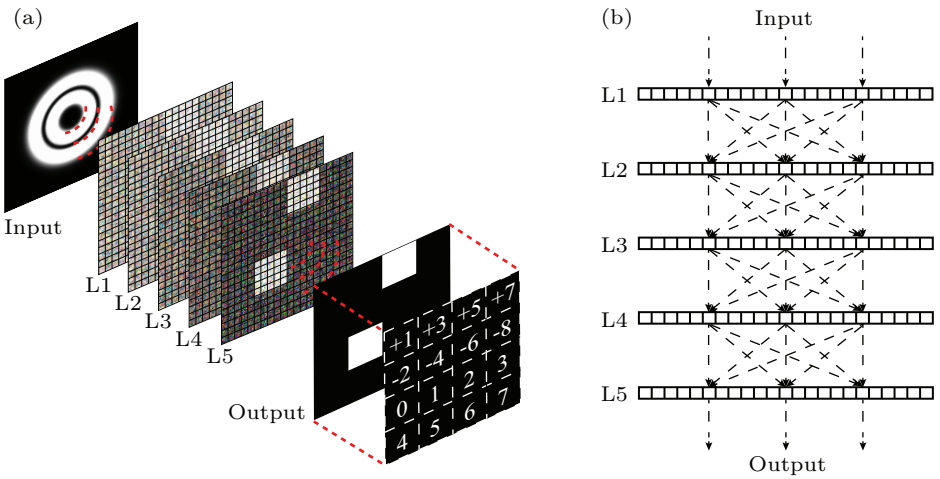


Fig. 1. Schematic diagram of the OAM mode recognition scheme based on DDNN. (a) The prediction of OAM mode recognition based on DDNN. (b) Fully connected structure and forward propagation between diffractive layers of DDNN.

The Fresnel diffraction theory can be used to simplify the propagation of light beams.[28] The frequency domain distribution of the incident beam on the $(N-1)^{\text{th}}$ layer can be obtained by Fourier transform of electric field distribution in the spatial domain, as expressed by the following equation:

$$U_{z_{N-1}}^{N-1}(f_x,f_y)=F\left(u_{z_{N-1}}^{N-1}(x_{N-1},y_{N-1})\right), \tag{3}$$

where $u_{z_{N-1}}^{N-1}(x_{N-1},y_{N-1})$ is the electric field distribution of the incident beam, z_{N-1} denotes the observation plane on the propagation axis, F represents the Fourier transform. Thus, the output of the $(N-1)^{\text{th}}$ diffraction layer can be expressed as

$$U_{z_{N-1}}^{N-1}(f_x,f_y)=F[u_{z_{N-1}}^{N-1}(x_{N-1},y_{N-1})\times t_{z_{N-1}}^{N-1}(x_{N-1},y_{N-1})]. \tag{4}$$

According to the Fresnel diffraction theory, the beam propagates to the N^{th} diffractive layer, and the electric field distribution in the spatial domain can be given as

$$u_{z_N}^{N}(x_N,y_N)=F^{-1}\left(U_{z_{N-1}}^{N-1}(f_x,f_y)\times H(f_x,f_y)\right), \tag{5}$$

where F^{-1} is the reverse Fourier transform. $H(f_x,f_y)=\exp[\mathrm{j}k(z_N-z_{N-1})]\exp\left[-\mathrm{j}\pi\lambda(z_N-z_{N-1})\left(f_x^2+f_y^2\right)\right]$ represents the transform function, with $k=2\pi/\lambda$ representing the wave number and (z_N-z_{N-1}) the separation distance between the diffractive layers.

The OT can be simulated using several separate phase screens produced by power spectrum inversion method, where each phase screen is a thin sheet that adjusts the phase of the beam.[29] The OT-induced perturbation effects can be handled separately for propagation and phase perturbations by a step-by-step approach. At each step, the phase perturbation caused by refractive index fluctuations is achieved by multiplying the input field by a phase exponential function (phase screen), and then the beam propagates in free space between two adjacent phase screens. The phase screen is statistically independent of the spatial statistics matched to refractive index fluctuations.[30] The refractive index fluctuation spectrum of homogeneous and isotropic OT can be expressed as

$$\begin{aligned}\Phi_{\text{ot}}(\kappa) &= 0.388C_n^2\kappa^{-11/3}[1+2.35(\kappa\eta)^{2/3}]\\ &\times[\exp(-A_{\text{T}}\delta)-2\tau^{-1}\exp(-A_{\text{TS}}\delta)\\ &+\tau^{-2}\exp(-A_{\text{S}}\delta)],\end{aligned} \tag{6}$$

where C_n^2 is a measure of the strength of ocean fluctuations, κ is the spatial frequency, η is the Kolmogorov microscale (inner scale), τ is the balance parameter that means the relative strength of temperature and salinity fluctuations, which ranges from -5 to 0. $A_{\text{T}}=1.863\times10^{-2}$, $A_{\text{S}}=1.9\times10^{-4}$, $A_{\text{TS}}=9.41\times10^{-3}$, and $\delta=8.284(\kappa\eta)^{4/3}+12.978(\kappa\eta)^2$. The phase spectrum can be expressed as

$$\Phi(\kappa)=2\pi k_0^2 Z\Phi_{\text{ot}}(\kappa), \tag{7}$$

where k_0 represents the wave number of the incident beam. Z denotes the propagation distance. The phase screen can be obtained by the Fourier transform

$$\varphi(x,y)=F\left[C\left(\frac{2\pi}{N\Delta x}\right)\sqrt{\Phi(\kappa)}\right], \tag{8}$$

where F represents the Fourier transformation, C denotes an $N\times N$ array of complex random numbers with 0 mean and variance 1, and Δx is the grid spacing.

2.2. Data preparing

In this work, we select 12 kinds of OAM modes with different azimuthal and radial indices, including $\{\ell=+1,p=7\},\{\ell=+3,p=5\},\{\ell=+3,-2,p=7\},\{\ell=+5,-6,p=0\},\{\ell=+1,p=2,3\},\{\ell=+3,p=5,6\},\{\ell=+7,p=3\},\{\ell=-6,p=0\},\{\ell=-2,-4,p=2\},\{\ell=+1,+3,p=3\},\{\ell=-4,p=3,4\},\{\ell=-8,p=6,7\}$. Figure 2 shows the intensity patterns and the corresponding ideal outputs for different OAM modes.

We utilize LabVIEW 2012 to simulate and acquire the intensity distribution images of OAM modes. The OAM beam's wavelength is 633 nm, and the pixel size of phase plate is 128×128. The DDNN model extracts the features of the OAM mode intensity distribution through training and performs classification. Therefore, in the simulation, the wavelengths of different OAM beams and the pixel size of the phase plate do not affect the feature extraction of the OAM beam intensity distribution by the DDNN model. For each class of OAM mode, we select 6000 intensity patterns, of which 5000 intensity patterns are used as the training dataset and 1000 intensity patterns are used as the test set. The ideal output is marked as ground truth as a label for each kind of OAM mode. In order to facilitate DDNN model training, the intensity patterns obtained from LabVIEW 2012 are resized to 128×128, converted to gray scale images and normalized. Our training is implemented with the Tensorflow framework on four NVIDIA TITAN RTX GPUs. The distance between diffractive layers is 0.1 m, and the DDNN model is trained for 30 epochs using the Adam optimizer[31] with a learning rate of 0.01. The error backward propagation algorithm and Adam gradient descent optimizer are used to train the DDNN model to ensure the convergence of the model and make the model output consistent with the ideal output (ground truth). The loss function can be defined as

$$\text{loss}=\left(u_{\text{o}}-u_{\text{gt}}\right)^2, \tag{9}$$

where u_{o} and u_{gt} represent the actual output of DDNN and ideal output, respectively.

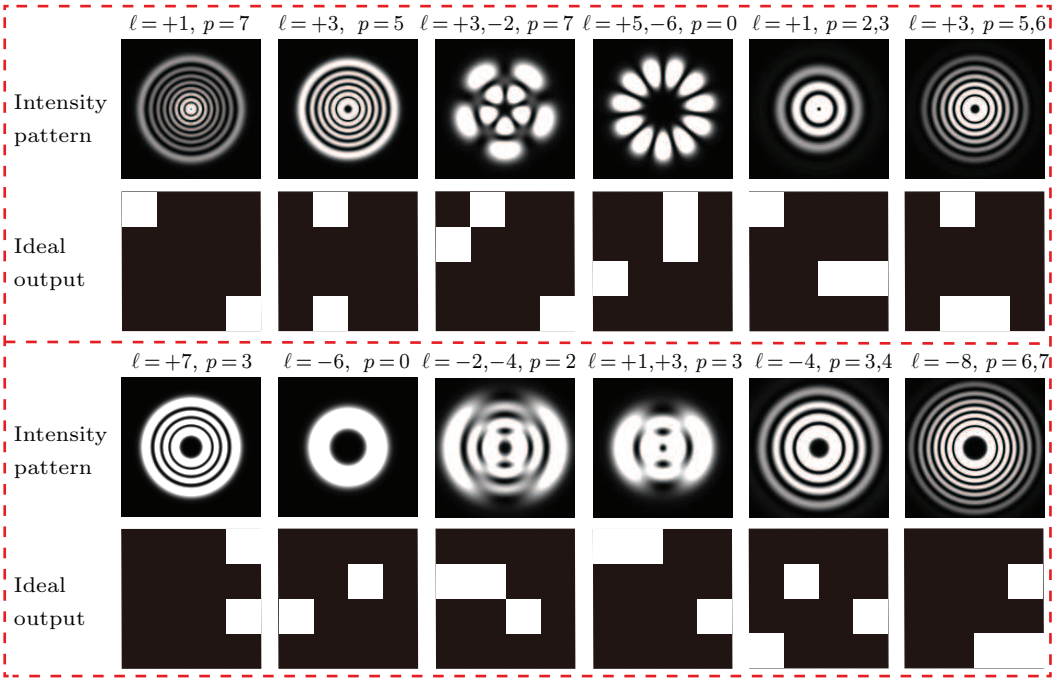


Fig. 2. The intensity patterns and corresponding ideal outputs for different OAM modes ($\{\ell=+1, p=7\}$, $\{\ell=+3, p=5\}$, $\{\ell=+3,-2, p=7\}$, $\{\ell=+5,-6, p=0\}$, $\{\ell=+1, p=2,3\}$, $\{\ell=+3, p=5,6\}$, $\{\ell=+7, p=3\}$, $\{\ell=-6, p=0\}$, $\{\ell=-2,-4, p=2\}$, $\{\ell=+1,+3, p=3\}$, $\{\ell=-4, p=3,4\}$, $\{\ell=-8, p=6,7\}$).

3. Performance evaluation

The number of diffractive layers is an important parameter that affects the performance of the DDNN model. We compare the effect of different diffraction layers on the recognition accuracy of the DDNN model, as shown in Fig. 3. Within 30 epochs, with the increase of epoch, the recognition accuracy gradually increases and tends to be stable. At the same time, with the increase of the number of diffraction layers, the recognition accuracy also improves significantly. Without the interference of OT, the recognition accuracy of the DDNN model with five diffractive layers reaches 1.

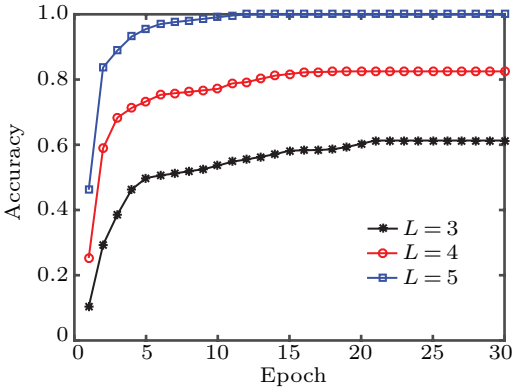


Fig. 3. The recognition accuracy of the DDNN model with different diffraction layers.

We choose a DDNN model with 5 diffractive layers to establish a mode recognition scheme for OAM beams. Depending on the modulation type of the DDNN, the amplitude and phase planes of each diffractive layer are changed during model training. When the DDNN model is optimal, the difference between the output result and the ideal output is the smallest, and the recognition accuracy reaches peak value. To evaluate the impact of OT on the performance of the DDNN-based OAM mode recognition scheme, we analyze the variation of model recognition accuracy under different OT strengths. We choose four levels of OT strength, where $C_n^2 = 1\times10^{-15}$ K$^2\cdot$m$^{-2/3}$ and $C_n^2 = 1\times10^{-12}$ K$^2\cdot$m$^{-2/3}$ represent the weak turbulence and the strong turbulence, respectively. Figure 4 shows the variation of the recognition accuracy of the DDNN-based OAM mode recognition scheme with epoch under different OT strengths. As the OT strength increases, the recognition accuracy of the DDNN model decreases. In a weak turbulence environment, the recognition accuracy of the DDNN model is less disturbed by turbulence, and its accuracy peaks at 1 after about 15 epochs. However, in a strong turbulence environment, the phase of the OAM mode is greatly affected by the turbulence, and the intensity pattern is distorted. Meanwhile, the recognition accuracy of the DDNN model will be reduced, and the maximum value is only 0.825.

Figure 5 shows the recognition accuracy of the DDNN-based OAM recognition scheme under different propagation distances in different OT strengths. As can be seen from Fig. 5, as the link distance increases, the recognition accuracy of the DDNN model under different OT strengths gradually decreases. In addition, in a specific propagation distance, as the OT strength increases, the recognition accuracy of the

DDNN model also decreases. At the weak OT strength $C_n^2 = 1 \times 10^{-15}$ $\mathrm{K}^2 \cdot \mathrm{m}^{-2/3}$, the recognition accuracy of the DDNN model reaches 1 at a link distance of 20 m, but only 0.801 at 50 m. At the strong OT strength $C_n^2 = 1 \times 10^{-12}$ $\mathrm{K}^2 \cdot \mathrm{m}^{-2/3}$, the recognition accuracy of the DDNN model is 0.825 at a link distance of 20 m, and only 0.514 at 50 m.

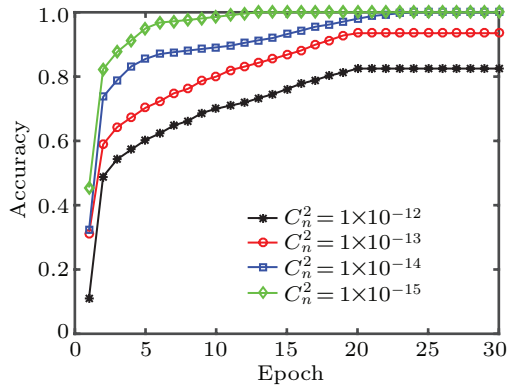


Fig. 4. The change curve of recognition accuracy of the OAM recognition scheme based on DDNN with different OT strengths.

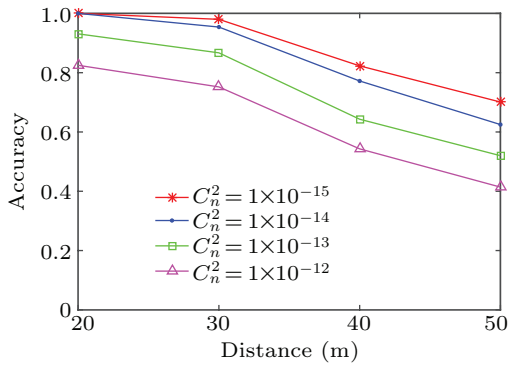


Fig. 5. The recognition accuracy of the OAM recognition scheme based on DDNN under different propagation distances in different OT strengths.

In fact, some works utilize CNN models to identify OAM modes. We evaluate the performance of DDNN-based and CNN-based OAM recognition schemes. Considering the influence of various aspects, we train both models for the same number of epochs on the same computer. Figure 6 shows the effect of different OT strengths on the recognition accuracy of DDNN-based and CNN-based OAM recognition schemes. As the OT strength increases, the recognition accuracy of the two schemes decreases. In a weak OT environment, the schemes based on DDNN and CNN models can achieve the recognition task with an accuracy of 1. However, in a strong OT environment, the accuracy of the DDNN-based OAM recognition scheme drops to 0.825, while the accuracy of the CNN-based OAM recognition scheme is only 0.732. It is obvious that OAM recognition schemes based on DDNN and CNN models can perform well under weak OT, but in strong OT, the recognition accuracy of the former is higher than that of the latter, which shows that the OAM recognition scheme based on DDNN has certain anti-OT characteristics.

Figure 7 shows the effect of different OT strengths on the calculation time of DDNN-based and CNN-based OAM recognition schemes. We use the trained DDNN and CNN models for classification, and record the calculation time of the two models, while the pre-data preparation and model training time are not recorded. It can be seen from Fig. 7 that the calculation time of DDNN and CNN models does not increase with the increase of OT strength. The calculation time of the DDNN model is about 1.672 s, while the computation time of the CNN model is about 4.286 s, which means that the DDNN model is better than the CNN model in terms of time cost.

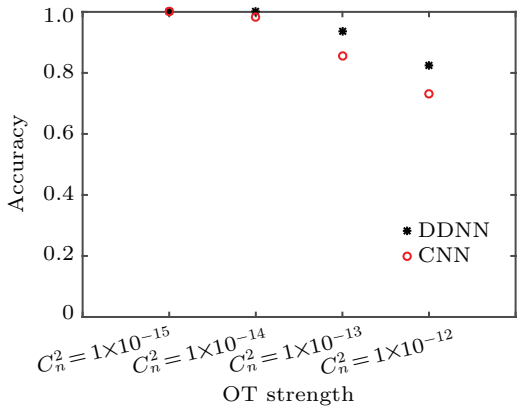


Fig. 6. The recognition accuracy of OAM mode recognition schemes based on DDNN and CNN under different OT strengths.

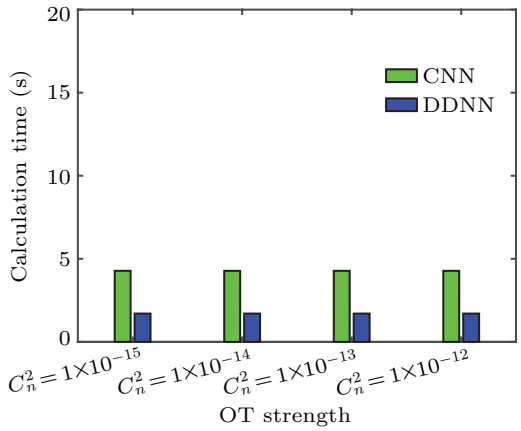


Fig. 7. The calculation time of OAM mode recognition schemes based on DDNN and CNN under different OT strengths.

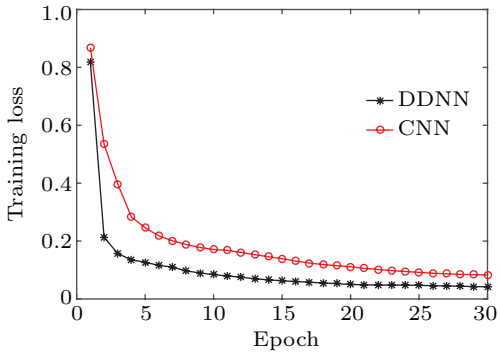


Fig. 8. The training loss of the OAM mode recognition scheme based on DDNN and CNN within 30 epochs.

The loss function can be used to evaluate the difference between the actual output and the ideal output, and can also be used to reflect the pros and cons of the training model. Figure 8 shows the variation of training loss for DDNN and CNN models within 30 epochs. With the increase of epoch, the training loss of both DDNN and CNN models gradually decreases and tends to be stable. When the epoch is 25, the training loss of the DDNN model basically reaches the minimum value of 0.047, while the training loss of the CNN model is 0.092. The DDNN model converges faster than the CNN model, and the training loss value is lower than the CNN model.

4. Conclusion

In summary, we have proposed a DDNN-based OAM mode recognition scheme. The dataset includes intensity patterns of 12 classes of OAM modes, the DDNN model has been trained to recognize the azimuthal and radial indices of different OAM modes. The results show that when there is no OT interference, the recognition accuracy of the DDNN model can reach 1. The proposed scheme can accurately recognize the azimuthal and radial indices of OAM modes after short-distance propagation. When the propagation distance is greater than 50 m, the recognition accuracy will drop significantly. In addition, at the weak OT strength $C_n^2 = 1 \times 10^{-15}$ $\mathrm{K}^2 \cdot \mathrm{m}^{-2/3}$, the recognition accuracy of the DDNN model can also reach 1, which means that the DDNN-based OAM mode recognition scheme has characteristics resistant to turbulence interference. At the strong OT strength $C_n^2 = 1 \times 10^{-12}$ $\mathrm{K}^2 \cdot \mathrm{m}^{-2/3}$, the recognition accuracy of the DDNN model is 0.825, while the recognition accuracy of the CNN model is only 0.732, which indicates that the robustness of the DDNN model is better than that of the CNN model. The calculation time of the DDNN-based OAM mode recognition scheme is also less than that of the CNN-based OAM mode recognition scheme. In conclusion, the proposed scheme is combined with an all-optical passive diffractive layer to construct a DDNN to recognize the modes of OAM beams. The OAM mode recognition scheme based on DDNN can provide help for the development of UWOC systems in the future.

Acknowledgements

Project supported by the National Natural Science Foundation of China (Grant Nos. 61871234 and 62001249), and the Postgraduate Research and Practice Innovation Program of Jiangsu Province, China (Grant No. KYCX200718).

References

[1] Chen L K, Shao Y J and Di Y J 2022 *J. Lightw. Technol.* **40** 1440
[2] Kumar S, Prince S and Kumar G S 2021 *Photon. Netw. Commun.* **41** 163
[3] Zhao M M, Li X N, Chen X, Tong Z J, Lyu W C, Zhang Z J and Xu J 2020 *Opt. Express* **28** 34450
[4] Sun X B, Kang C H, Kong H W, Alkhazragi O, Guo Y J, Ouhssain M, Weng Y, Jones B H, Ng T K and Ooi B S 2020 *J. Lightw. Technol.* **38** 421
[5] Zeng Z Q, Fu S, Zhang H H, Dong Y H and Cheng J L 2017 *IEEE Commun. Surv. Tutorials* **19** 204
[6] Lv Z J, He G, Qiu C F and Liu Z J 2021 *IEEE Photon. J.* **13** 7300508
[7] Oubei H M, Duran J R, Janjua B, Wang H Y, Tsai C T, Chi Y C, Ng T K, Kuo H C, He J H, Alouini M S, Lin G R and Ooi B S 2015 *Opt. Express* **23** 23302
[8] Liu D J, Wang Y C, Wang G Q, Yin H M and Zhong H Y 2019 *Chin. Phys. B* **28** 104207
[9] Allen L, Beijersbergen M W, Spreeuw R J C and Woerdman J P 1992 *Phys. Rev. A* **45** 8185
[10] Sun Z C, Yan M Y and Xun B J 2020 *Chin. Phys. B* **29** 104101
[11] Cui C, Wang Z, Li Q, Wu C Q and Wang J 2019 *Acta Phys. Sin.* **68** 064211 (in Chinese)
[12] Zhao Y, Yang C X, Zhu J X, Lin F, Fang Z Y and Zhu X 2020 *Chin. Phys. B* **29** 067301
[13] Wang H G, Song Q Y, Cai Y, Lin Q G, Lu X W, Shangguan H C, Ai Y X and Xu S X 2020 *Chin. Phys. B* **29** 097404
[14] Wang W, Wang P, Cao T, Tian H X, Zhang Y and Guo L X 2017 *IEEE Photon. J.* **9** 7905315
[15] Ruffato G, Rossi R, Massari M, Mafakheri E, Capaldo P and Romanato F 2017 *Sci. Rep.* **7** 18011
[16] Lei T, Zhang M, Li Y R, Jia P, Liu G N, Xu X G, Li Z H, Min C J, Lin J, Yu C Y, Niu H B and Yuan X C 2015 *Light Sci. Appl.* **4** e257
[17] Stegenburgs E, Bertoncini A, Trichili A, Alias M S, Ng T K, Alouini M S, Liberale C and Ooi B S 2019 *IEEE Commun. Mag.* **57** 65
[18] Mazilu M, Mourka A, Vettenburg T, Wright E M and Dholakia K 2012 *Appl. Phys. Lett.* **100** 231115
[19] Guo Z Y, Wang Z K, Dedo M I and Guo K 2018 *IEEE Photon. J.* **10** 7906511
[20] Cui X Z, Yin X L, Chang H, Liao H Y, Chen X Z, Xin X J and Wang Y J 2019 *Opt. Commun.* **452** 116
[21] Wei X Q, Wang P P, Zene Z J, Huang Z B, Zhu X X, Liu J M, Li Y, Chen S Q and Fan D Y 2020 *Acta Phys. Sin.* **69** 014209 (in Chinese)
[22] Dedo M I, Wang Z K, Guo K and Guo Z Y 2020 *Opt. Commun.* **456** 124696
[23] Lu C D, Tian Q H, Xin X J, Liu B, Zhang Q, Wang Y J, Tian F, Yang L J and Gao R 2020 *Opt. Express* **28** 37936
[24] Zhang L F, Lin Y Y, She Z Y, Huang Z H, Li J Z, Luo X J, Yan H, Huang W, Zhang D W and Zhu S L 2021 *Phys. Rev. A* **104** 053525
[25] Lin X, Rivenson Y, Yardimci N T, Veli M, Luo Y, Jarrahi M and Ozcan A 2018 *Science* **361** 1004
[26] Zhan H C, Peng Y X, Chen B, Wang L, Wang W N and Zhao S M 2022 *Opt. Express* **30** 23305
[27] Qian C, Lin X, Lin X B, Xu J, Sun Y, Li E P, Zhang B L and Chen H S 2020 *Light Sci. Appl.* **9** 59
[28] Huang Z B, Wang P P, Liu J M, Xiong W J, He Y L, Xiao J N, Ye H P, Li Y, Chen S Q and Fan D Y 2021 *Phys. Rev. Appl.* **15** 014037
[29] Zhan H C, Wang L, Wang W N and Zhao S M 2021 *Optik* **240** 166990
[30] Zhan H C, Wang L and Wang W N 2022 *J. Lightw. Technol.* **40** 4129
[31] Kingma D P and Ba J L 2015 arXiv:1412.6980 [cs.LG]